

## Video Article

# Monovalent Cation Doping of $\text{CH}_3\text{NH}_3\text{PbI}_3$ for Efficient Perovskite Solar Cells

Mojtaba Abdi-Jalebi<sup>1</sup>, M. Ibrahim Dar<sup>2</sup>, Aditya Sadhanala<sup>1</sup>, Satyaprasad P. Senanayak<sup>1</sup>, Michael Grätzel<sup>2</sup>, Richard H. Friend<sup>1</sup><sup>1</sup>Cavendish Laboratory, University of Cambridge<sup>2</sup>Institute of Chemical Sciences and Engineering, École Polytechnique Fédérale de LausanneCorrespondence to: Mojtaba Abdi-Jalebi at [ma571@cam.ac.uk](mailto:ma571@cam.ac.uk)URL: <https://www.jove.com/video/55307>DOI: [doi:10.3791/55307](https://doi.org/10.3791/55307)Keywords: Engineering, Issue 121, Monovalent cation halide, additives,  $\text{CH}_3\text{NH}_3\text{PbI}_3$  perovskite, doping, surface passivation

Date Published: 3/19/2017

Citation: Abdi-Jalebi, M., Dar, M.I., Sadhanala, A., Senanayak, S.P., Grätzel, M., Friend, R.H. Monovalent Cation Doping of  $\text{CH}_3\text{NH}_3\text{PbI}_3$  for Efficient Perovskite Solar Cells. *J. Vis. Exp.* (121), e55307, doi:10.3791/55307 (2017).

## Abstract

Here, we demonstrate the incorporation of monovalent cation additives into  $\text{CH}_3\text{NH}_3\text{PbI}_3$  perovskite in order to adjust the optical, excitonic, and electrical properties. The possibility of doping was investigated by adding monovalent cation halides with similar ionic radii to  $\text{Pb}^{2+}$ , including  $\text{Cu}^+$ ,  $\text{Na}^+$ , and  $\text{Ag}^+$ . A shift in the Fermi level and a remarkable decrease of sub-bandgap optical absorption, along with a lower energetic disorder in the perovskite, was achieved. An order-of-magnitude enhancement in the bulk hole mobility and a significant reduction of transport activation energy within an additive-based perovskite device was attained. The confluence of the aforementioned improved properties in the presence of these cations led to an enhancement in the photovoltaic parameters of the perovskite solar cell. An increase of 70 mV in open circuit voltage for AgI and a 2  $\text{mA}/\text{cm}^2$  improvement in photocurrent density for NaI- and CuBr-based solar cells were achieved compared to the pristine device. Our work paves the way for further improvements in the optoelectronic quality of  $\text{CH}_3\text{NH}_3\text{PbI}_3$  perovskite and subsequent devices. It highlights a new avenue for investigations on the role of dopant impurities in crystallization and controls the electronic defect density in perovskite structures.

## Video Link

The video component of this article can be found at <https://www.jove.com/video/55307/>

## Introduction

Currently, the dominant portion of the world's energy requirement (*i.e.*, 85%) is being supplied by the combustion of oil, coal, and natural gas, which facilitates global warming and has deleterious effects on our environment<sup>1</sup>. Therefore, the development of  $\text{CO}_2$ -neutral sources of energy is of paramount interest. Photovoltaics (PV) is an ideal energy conversion process that can meet this requirement. However, cost and efficiency, as the main obstacles to the extensive adoption of PV technology, must be improved. Emerging PV technologies based on new materials, such as perovskite solar cells (PSC), have the combination of lower cost and greater efficiency. This is achieved through the utilization of cheap materials that are readily available, as well as through fast, facile, and low-energy processing routes compared to silicon-based counterparts<sup>2,3,4</sup>. A remarkable improvement in the power conversion efficiency (PCE), from 3.8% to more than 22%, has been reported for hybrid organic-inorganic lead halide perovskite since its first appearance in PV architecture<sup>5,6,7,8</sup>. Such a superb performance originates from the strong light absorption with an extremely sharp band-edge, the very low energetic disorder, the weakly-bound excitons that easily dissociate into free carriers with large diffusion lengths, and the photon recycling capability of hybrid organic-inorganic lead halide perovskite<sup>9,10,11,12</sup>. These materials are categorized in the perovskite family, which are crystallized from organic halide and metal halide salts to form crystals in the  $\text{ABX}_3$  structure, where X is an anion and A and B are cations of different sizes (A being larger than B). Reported cations for the A site include methylammonium (MA), formamidinium (FA), and cesium (Cs); a combination of these cations shows the highest performance<sup>13,14</sup>. Furthermore, the main candidate for the divalent cation in the B site is lead, which can be replaced by tin; the bandgap can be successfully red-shifted to over 1,000 nm in a lead-tin mixed perovskite<sup>15</sup>. Similarly, the X-site occupants have been studied extensively, where a mixture of iodide (I) and bromide (Br) were introduced as the main candidates<sup>16,17</sup>. Therefore, it is highly plausible to manipulate the structural, morphological, and optoelectronic properties of perovskites by altering their chemical composition.

Despite the fact that the enhanced crystalline quality and the macroscopic uniformity of the perovskite film are key parameters to achieve efficient devices<sup>18</sup>, the impact of the boundaries between the polycrystalline domains, the origin and role of electronic defects in the perovskite absorbers, and the role of the charge collection layers upon loss processes in the perovskite solar cells are not yet well understood. Regarding the nature of electronic defects in the perovskite structure, it has been reported that many of the defects, such as I or Pb vacancies, result in states that are very close to or within the continuum of states in the conduction and valence bands, which might have a negative electronic impact on the photovoltaic devices<sup>19</sup>. In addition, a strong covalent bonding interaction between lead cations and iodide anions in the perovskite plane may lead to the existence of intrinsic defects (*e.g.*, under-coordinated Pb dimers and I trimers), which could create sites within the band-edge that act as charge recombination centers during the operation of the device<sup>20</sup>.

Here, we investigate the impact of doping  $\text{CH}_3\text{NH}_3\text{PbI}_3$  perovskite with monovalent cation halides, including  $\text{Na}^+$ ,  $\text{Cu}^+$ , and  $\text{Ag}^+$ , lower-valence metal ions than  $\text{Pb}^{2+}$ . We therefore incorporate these cations through the addition of a rational amount of their halide-based salts (*e.g.*, NaI, CuBr, CuI, and AgI) into the perovskite precursor solution. These cations have ionic radii similar to  $\text{Pb}^{2+}$ , so substitutional doping within the

crystal is probable. We have shown that the presence of these cations strongly affects both the morphology and coverage of the perovskite layer. In addition, the presence of these cations (e.g.,  $\text{Na}^+$  and  $\text{Ag}^+$ ) has been confirmed by X-ray photoelectron spectroscopy (XPS), and a significant change in the Fermi level of perovskite was measured by Kelvin probe force microscopy (KPFM). By incorporating these cations into sequentially deposited perovskite solar cells, we achieved an improvement in the photovoltaic efficiency of PSC (15.6% compare to 14%). Therefore, it is very essential to enhance the structural and optoelectronic properties of the absorber layer (e.g., perovskite) in solar cell architecture to maximize the charge transport and to passivate the surface traps in order to reach the highest PV performance.

## Protocol

### 1. Synthesis and Deposition of Pristine and Additive-based $\text{CH}_3\text{NH}_3\text{PbI}_3$

NOTE: All the solutions were prepared inside an argon glove box under moisture- and oxygen-controlled conditions ( $\text{H}_2\text{O}$  level: <1 ppm and  $\text{O}_2$  level: <10 ppm).

1. Dissolve 553 mg (1.2 M) of  $\text{PbI}_2$  in 1 mL of *N,N*-dimethylformamide (DMF) under constant stirring at 80 °C.
2. Add 0.02 M of monovalent cation halides to the  $\text{PbI}_2$  solution.
3. Spin-coat the resulting yellow transparent solution onto the substrate (e.g., mesoporous- $\text{TiO}_2$ ) for 30 s at 6,500 rpm with a ramp of 4,000 rpm.
4. Bake the films on a hotplate at 80 °C for 30 min.
5. Dissolve 40 mg of methylammonium iodide (MAI) in 5 mL of isopropanol.
6. Spin-coat a sufficient amount of MAI solution onto the resulting lead iodide films using a two-step protocol that includes 45 s of loading time followed by 20 s of spinning at 4,000 rpm.
7. Anneal the spin-coated perovskite films on a hotplate at 100 °C for 45 min.

### 2. Solar Cell Fabrication

#### 1. Substrate preparation

1. Pattern fluorine-doped tin oxide (FTO)-coated glass.
  1. Cover the active area of the FTO glass with semitransparent adhesive tape.
  2. Pour the zinc (Zn) powder on the uncovered areas of the FTO substrates.
  3. Prepare 2 M of hydrochloric acid (HCl) in distilled water.
  4. Pour the HCl solution onto the part of the FTO glass that is covered with Zn powder.
  5. Wash the FTO with water and remove the tape.
2. Cleaning the substrates
  1. Wash the FTO glass using 2% (w/v) detergent.
  2. Sonicate the etched FTO substrates in acetone and isopropanol (IPA) for 10 min.
  3. Treat the FTO substrates with an ultraviolet/ $\text{O}_3$  cleaner for 15 min.

#### 2. Deposition of a hole blocking layer

1. Add 0.6 mL of titanium diisopropoxide bis(acetylacetonate) (TAA) in 7 mL of IPA.
2. Put the cleaned and patterned FTO substrates on a hotplate at 450 °C and cover the contact area before heating.
3. Spray pyrolysis the TAA solution onto the uncovered area using  $\text{O}_2$  as the carrier gas.
4. Leave the samples at 450 °C for 30 min.

#### 3. Deposition of an electron transport layer

1. Dilute the commercial  $\text{TiO}_2$  paste (30-nm particle size) with ethanol (2:7, weight ratio).
2. Homogenize the  $\text{TiO}_2$  dilution by sonicating for 30 min.
3. Spin-coat the titania dilution onto the prepared samples with compact  $\text{TiO}_2$  layers for 30 s at 5,000 rpm with a ramp of 2,000 rpm.
4. Anneal the titania films at 500 °C for 30 min.
5. Treat the resulting mesoporous  $\text{TiO}_2$  films in a 40 mM solution of  $\text{TiCl}_4$  in distilled water at 70 °C for 20 min.
6. Anneal the  $\text{TiCl}_4$ -treated films at 450 °C for 30 min.

#### 4. Deposition of the perovskite layer

NOTE: The FTO substrates with titania layers were transferred to a dry-air box with a humidity of <1% for the rest of the fabrication process.

1. Spin-coat the prepared lead iodide solutions (with and without dopants) onto the mesoporous  $\text{TiO}_2$  for 30 s at 6,500 rpm with a ramp of 4,000 rpm.
2. Bake the films on a hotplate at 80 °C for 30 min.
3. Spin-coat a sufficient amount of MAI solution into the resulting lead iodide films using a two-step protocol that includes 45 s of loading time followed by spinning for 20 s at 4,000 rpm with a ramp of 2,000 rpm.
4. Anneal the spin-coated perovskite films on a hotplate at 100 °C for 45 min.

#### 5. Deposition of the hole transport layer

1. Add 72.3 mg of spiro-OMeTAD to 1 mL of chlorobenzene and shake until the solution becomes transparent.
2. Make a stock solution of bis(trifluoromethylsulphonyl)imide (LiTFSI) by adding 520 mg of LiTFSI in acetonitrile.
3. Add 17.5  $\mu\text{L}$  of the LiTFSI stock solution and 28.8  $\mu\text{L}$  of 4-*tert*-butylpyridine (TBP) to the spiro-OMeTAD solution.
4. Spin-coat the above solution for 30 s at 4,000 rpm with a ramp of 2,000 rpm.

#### 6. Thermal evaporation of the top contact

1. Mask the samples and put them in the vacuum chamber of the evaporator.
2. Evaporate 80 nm of gold at a rate of 0.01 nm/s.

## Representative Results

Field emission scanning electron microscopy (FESEM) was used to record both cross-sectional images of the fabricated perovskite solar cells (**Figure 1**) and top view images of the deposited  $\text{PbI}_2$  and  $\text{CH}_3\text{NH}_3\text{PbI}_3$  films (**Figure 2**). X-ray diffraction (XRD) and X-ray photoelectron spectroscopy (XPS) were employed to characterize the structural properties of the perovskite films (**Figures 3** and **4**). Photothermal deflection spectroscopy (PDS) and Kelvin probe force microscopy (KPFM) were used to probe the optical and electrical properties of the perovskite films, respectively (**Figures 5** and **6**). Furthermore, temperature-dependent bulk transport measurements based on space charge limited current (SCLC) was performed on the perovskite devices (**Figure 7**). Finally, a standard photovoltaic measurement of the fabricated devices was performed (**Figure 8** and **Table 1**).

Based on the top-view SEM images of the  $\text{PbI}_2$  and  $\text{CH}_3\text{NH}_3\text{PbI}_3$  deposited on the mesoporous  $\text{TiO}_2$  layer (mp- $\text{TiO}_2$ ) shown in **Figure 2**, the effect of the additives on the morphology of perovskite was illustrated where large branch-shaped crystals of  $\text{PbI}_2$  were achieved in the NaI-based sample. This led to the formation of larger asymmetric crystals of perovskite. Furthermore, we obtained a uniform and pinhole-free perovskite capping layer for CuI- and AgI-based samples (**Figure 2c** and **2e**). To investigate the effect of monovalent cation halide additives on the crystal structure of  $\text{CH}_3\text{NH}_3\text{PbI}_3$  and on the conversion of  $\text{PbI}_2$  into  $\text{CH}_3\text{NH}_3\text{PbI}_3$ , X-ray diffraction was performed (**Figure 3**). Although the crystal structure of the final perovskite remained the same for all samples, it is evident that the diffraction peak at  $2\theta = 12.6$ , which corresponds to the unconverted  $\text{PbI}_2$ , was eliminated in the presence of NaI and CuBr additives. In order to confirm the presence of these monovalent cations within the  $\text{CH}_3\text{NH}_3\text{PbI}_3$  perovskite films, we carried out an XPS analysis, as shown in **Figure 4**. On the basis of the XPS data, we demonstrated the presence of Na and Ag ions within the perovskite films, whereas the concentration of Cu could not be estimated, probably due to the nearness of iodide (I 3p $_{1/2}$ ) and copper (Cu 2p $_{1/2}$ ) peaks.

The effect of the monovalent cation additives on the absorption spectrum of the perovskite is shown in **Figure 5a**, which was measured by PDS. It is evident that the additive-based  $\text{CH}_3\text{NH}_3\text{PbI}_3$  had lower sub-bandgap absorption compared to the pristine sample. Furthermore, an absorption tail was observed for Cu-based samples, which originated from the intrinsic absorption of copper halide (**Figure 5b**). Although the absorption tail confirms the presence of Cu cations in the final perovskite films, it is evident, based on the comparison between the PDS of CuI-based  $\text{PbI}_2$  and  $\text{CH}_3\text{NH}_3\text{PbI}_3$ , that their incorporation is not complete. In addition, the Urbach energy ( $E_u$ ), which is a measure of the degree of energetic disorder of a material, was estimated for pristine, NaI-, CuBr-, CuI-, and AgI-based perovskite, and the values are 15.6, 11.8, 12.8, 13.5, and 15.2 meV, respectively (inset of **Figure 5a**).

To explore the influence of the aforementioned additives on the electronic structure of  $\text{CH}_3\text{NH}_3\text{PbI}_3$ , we performed KPFM, where the contact potential difference (CPD) of the line profiles was measured. This corresponds to the surface work function ( $\Phi$ ) of the perovskite shown in **Figure 6**. A clear shift in the CPD (*i.e.*, 0.1 V) of additive-based perovskite compared to the pristine one shows that the perovskite Fermi level is shifted towards the valence band. This change in the Fermi level of perovskite can be attributed to either substitutional p-doping (*e.g.*, the replacement of  $\text{Pb}^{2+}$  with monovalent cations  $\text{X}^+$ ) or surface passivation at the crystalline surfaces of perovskite.

To investigate the effect of doping on the density of the charges and on their transport properties in  $\text{CH}_3\text{NH}_3\text{PbI}_3$ , we performed temperature-dependent bulk transport measurements (**Figure 7a**). We then estimated the bulk carrier mobility ( $\mu_{\text{SCL}}$ ) based on the space charge limited current (SCLC) of the complete electron and hole-only pristine and additive-based perovskite devices. A remarkable increase in the conductivity and in both the electron and hole mobilities were achieved, particularly for the NaI and CuBr samples compared to pristine perovskite (**Table 1**). It is notable that the improvement in the charge mobility and conductivity are consistent with the enhancement in the short circuit current ( $J_{\text{sc}}$ ) and fill factor (FF) of the fabricated solar cells shown in **Figure 7b**. Furthermore, we estimated the activation energy for charge transport ( $E_A$ ) for both the electron and the hole using temperature-dependent bulk transport measurements, where a clear decrease was achieved for additive-based perovskite. This improvement is attributed to the higher density of carriers because of doping and filling the transport traps, which results in a significant decline in the transport barrier.

We fabricated perovskite solar cells based on the aforementioned monovalent cation halides, the corresponding J-V curves, and the photovoltaic parameters that are summarized in **Figure 8a** and **Table 1**. A significant improvement in open circuit voltage was achieved for both CuI- (0.99 V) and AgI- (1.02 V) based solar cells because of the ideal surface coverage (**Figure 2c** and **2e**). Furthermore, a remarkable increase in the short circuit current ( $\approx 2 \text{ mA cm}^{-2}$ ) for CuBr- and NaI-based solar cells was attained, which can be ascribed to the full conversion of  $\text{PbI}_2$  into  $\text{CH}_3\text{NH}_3\text{PbI}_3$ . This improvement was confirmed by the incident photon-to-current conversion efficiency (IPCE) spectra shown in **Figure 8b**. Finally, higher power conversion efficiency (PCE) levels of 15.2%, 15.6%, and 15.3% were achieved for NaI-, CuBr-, and CuI-based devices, respectively, compare to the 14.0% value for the pristine perovskite solar cell.

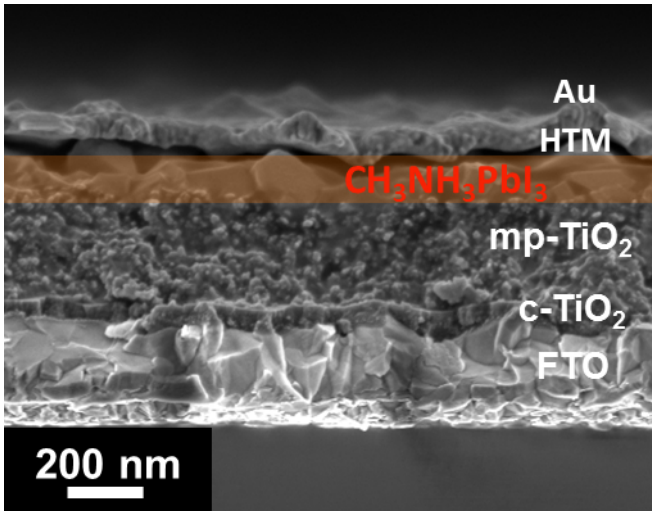


**Figure 1: Mesoscopic perovskite solar cell architecture.** SEM cross-sectional micrograph of a complete device with the following structure: FTO/compact-TiO<sub>2</sub>/mesoporous-TiO<sub>2</sub>/CH<sub>3</sub>NH<sub>3</sub>PbI<sub>3</sub>/Spiro-OMeTAD/Au.

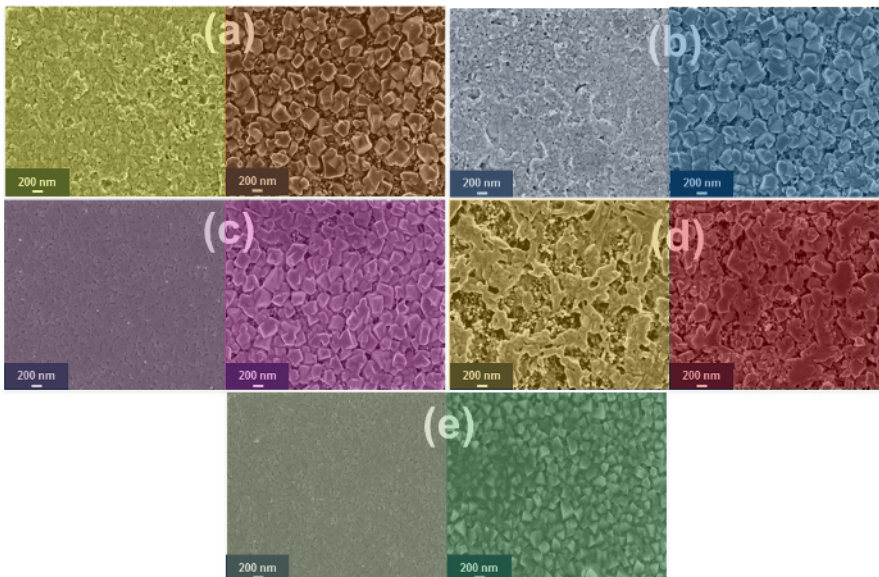


**Figure 2: Morphological analysis of lead iodide and perovskite structures.** Top-view SEM images of Pbl<sub>2</sub> (left side) and CH<sub>3</sub>NH<sub>3</sub>PbI<sub>3</sub> (right side) structures: (a) pristine, (b) CuBr-, (c) CuI-, (d) NaI-, and (e) AgI-based perovskite samples deposited on a mesoporous TiO<sub>2</sub>-coated FTO. This figure has been reproduced from reference<sup>18</sup>. [Please click here to view a larger version of this figure.](#)

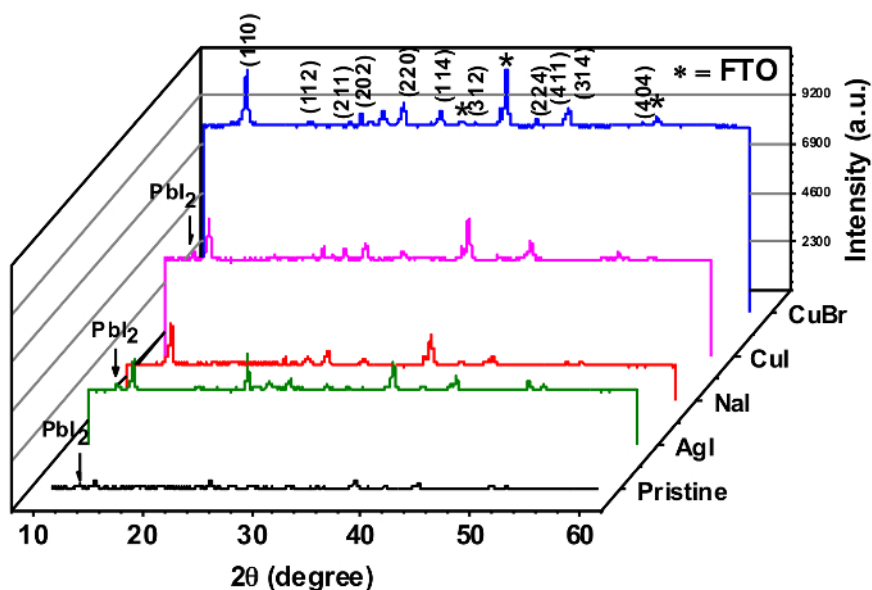


**Figure 3: Effect of monovalent cation halide additives on perovskite crystallinity.** X-ray diffraction spectra of pristine and additive-based  $CH_3NH_3PbI_3$  perovskite that is grown on mesoporous  $TiO_2$  film, which is deposited on the FTO-coated glass. This figure has been reproduced from reference<sup>18</sup>. [Please click here to view a larger version of this figure.](#)

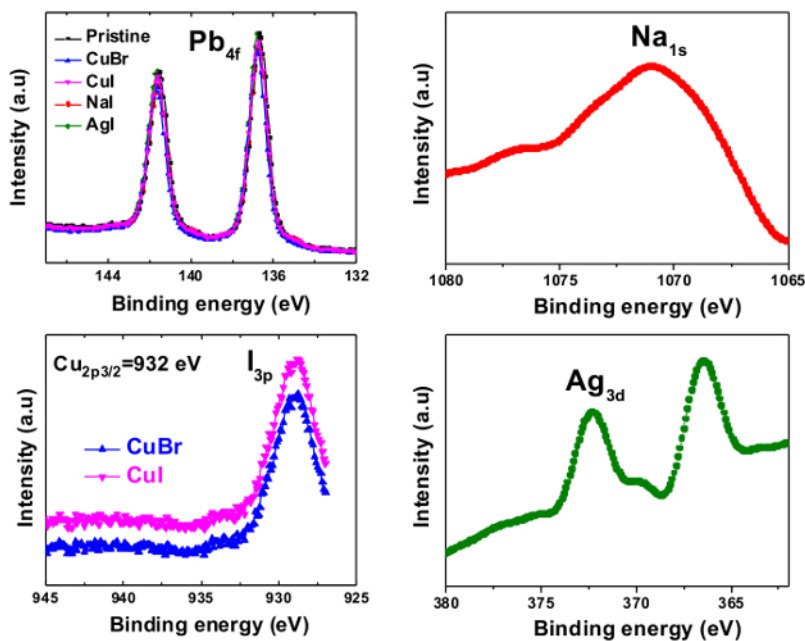


**Figure 4: Trace of monovalent cations in the  $CH_3NH_3PbI_3$  perovskite structure.** XPS analysis of pristine, CuBr-, CuI-, NaI-, and AgI-based perovskite films. This figure has been reproduced from reference<sup>18</sup>. [Please click here to view a larger version of this figure.](#)

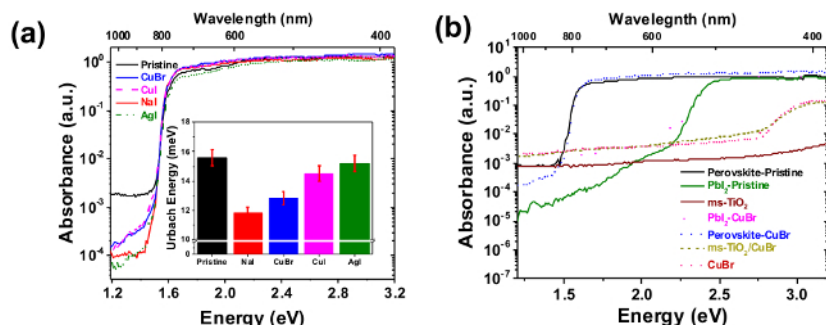


**Figure 5: Optical properties of perovskite films.** (a) The absorption spectra of perovskite films derived from pristine and additive-based lead sources measured using the PDS technique. The inset shows the corresponding Urbach energies for all samples. The error bar is defined by the SD in fitting the Urbach tail. (b) Comparison of the PDS absorption spectra of pristine and CuBr-based lead iodide and perovskite films, as well as CuBr deposited on ms-TiO<sub>2</sub> and CuBr-only films. This figure has been reproduced from reference<sup>18</sup>. [Please click here to view a larger version of this figure.](#)

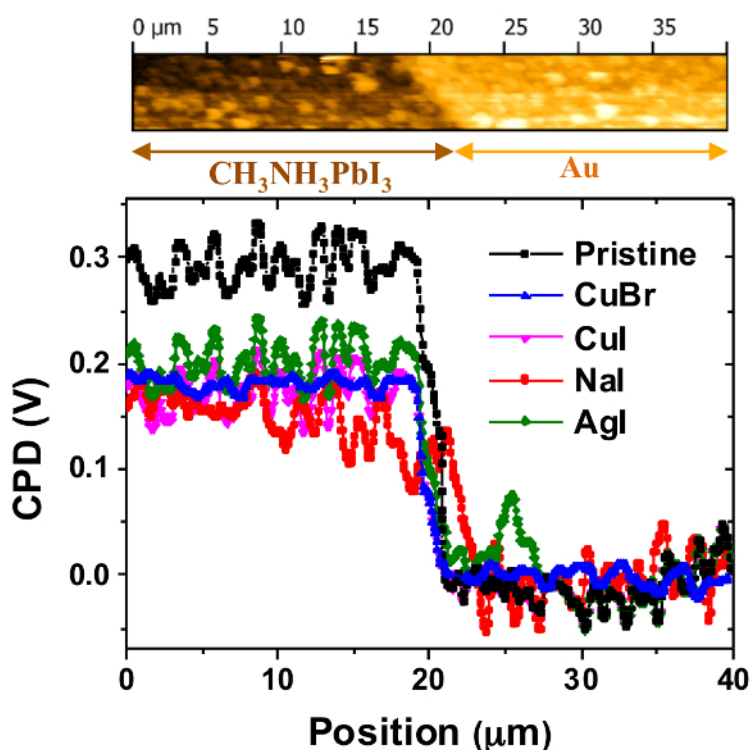


**Figure 6: Effect of monovalent cation additives on the surface potential of perovskite films.** CPD line profiles recorded from pristine and additive-based perovskite films using KPFM. The AFM topography image is shown on the top. This figure has been reproduced from reference<sup>18</sup>. [Please click here to view a larger version of this figure.](#)

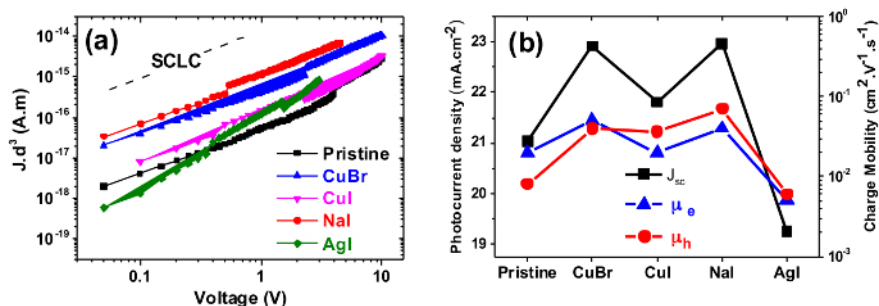


**Figure 7: Charge transport characteristics of perovskite films.** (a) J-V characteristics of hole-only devices (ITO/PEDOT:PSS/Perovskite/Au), utilized for estimating the SCLC hole mobility. Note that the current density (J) is scaled with the thickness of the perovskite layers. (b) The trends in the  $J_{sc}$ ,  $\mu_h$ , and  $\mu_e$  for pristine and additive-based perovskite. This figure has been reproduced from reference<sup>18</sup>. Please click here to view a larger version of this figure.

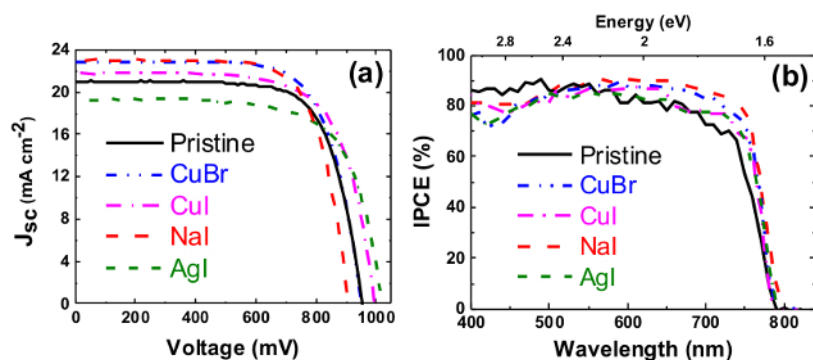


**Figure 8: Photovoltaic performance characteristics.** (a) Current-voltage characteristics of devices under an illumination of  $100 \text{ mW/cm}^2$ , obtained using different types of monovalent cation halides added to the lead source solution. (b) Incident photon-to-current efficiency (IPCE) spectra as a function of the wavelength of monochromatic light for the pristine, CuBr-, CuI-, NaI-, and AgI-based perovskite solar cells. This figure has been reproduced from reference<sup>18</sup>. Please click here to view a larger version of this figure.

| Type of Sample | $J_{sc}$<br>( $\text{mA cm}^{-2}$ ) | $V_{oc}$<br>(V) | FF   | PCE<br>(%) | $\mu_e$<br>( $\text{cm}^2/\text{Vs}$ ) | $\mu_h$<br>( $\text{cm}^2/\text{Vs}$ ) | $E_A^e$<br>(meV) | $E_A^h$<br>(meV) |
|----------------|-------------------------------------|-----------------|------|------------|--|--|------------------|------------------|
| Pristine       | 21.03                               | 0.95            | 0.70 | 14.01      | 0.02                                   | 0.008                                  | 135              | 198              |
| CuBr           | 22.92                               | 0.95            | 0.72 | 15.61      | 0.05                                   | 0.04                                   | 88               | 132              |
| CuI            | 21.81                               | 0.99            | 0.71 | 15.25      | 0.02                                   | 0.036                                  | 94               | 157              |
| NaI            | 22.97                               | 0.9             | 0.73 | 15.14      | 0.04                                   | 0.07                                   | 77               | 137              |
| AgI            | 19.24                               | 1.02            | 0.72 | 14.18      | 0.005                                  | 0.006                                  | 105              | 177              |

**Table 1: Photovoltaic and charge transport parameters of PSC.** Summary of the photovoltaic parameters derived from J-V measurements and charge mobilities, along with the activation energy for the pristine and additive-based perovskite solar cells that show the best performance and were fabricated using the two-step deposition method. It is notable that the statistics of the photovoltaic parameters follow the same trend as the best performing devices. This table has been reproduced from reference<sup>18</sup>.

## Discussion

A typical architecture of mesoscopic perovskite solar cells was used in this work, where a series of materials were spin-coated between a conductive substrate and a thermally-evaporated metal contact (Figure 1). The mesoporous  $\text{TiO}_2$  layers were treated with  $\text{TiCl}_4$ , which is reported to passivate the surface traps and to improve the interface between the electron transport layer and the absorber material<sup>21,22</sup>. The perovskite layer was then deposited using a sequential two-step deposition technique. The full conversion of lead halide into perovskite in the second step is essential to achieve the highest light absorption<sup>16,17</sup>, and we showed that the monovalent cation halide additives (e.g., NaI and CuBr) result in a complete conversion. Furthermore, the complete coverage of the mesoporous titania layer with the perovskite over-layer is vital to eliminate potential recombination between the hole transport layer (e.g., Spiro OMETAD) and the electron transport layer (e.g., mesoporous  $\text{TiO}_2$ )<sup>23</sup>. We illustrated that adding the monovalent cation halides (e.g., CuI and AgI) can improve the surface coverage of the perovskite capping layer, which leads to a higher open circuit voltage for the device.

The main advantage of our method is the doping step, where we incorporated monovalent cations into the  $\text{CH}_3\text{NH}_3\text{PbI}_3$  structure to improve the density of charges, the charge transport, and the conductivity of the absorber layer. As stated in the previous section, the aforementioned

dopants significantly enhanced both the electron and the hole mobilities. In addition, a remarkable decrease in the charge transport activation energy, as well as in the energetic disorder of the perovskite film, was achieved by monovalent cation doping.

In this work, we have demonstrated a method to dope  $\text{CH}_3\text{NH}_3\text{PbI}_3$  as an absorber layer in the mesoscopic perovskite solar cell structure. Monovalent cation halides were used to tune the morphological, optical, and electrical properties of  $\text{CH}_3\text{NH}_3\text{PbI}_3$  perovskite film in order to enhance the photovoltaic performance. Therefore, we incorporated three different monovalent cations (*i.e.*,  $\text{Na}^+$ ,  $\text{Cu}^+$ , and  $\text{Ag}^+$ ), which have similar ionic radii to  $\text{Pb}^{2+}$ , in the lead source in the sequential two-step deposition of  $\text{CH}_3\text{NH}_3\text{PbI}_3$ . As a result, a remarkable improvement in the structural and optoelectronic properties of  $\text{CH}_3\text{NH}_3\text{PbI}_3$  occurred in the presence of these additives, leading to higher PCEs for the fabricated solar cells. Therefore, our work highlights a facile way of doping the  $\text{CH}_3\text{NH}_3\text{PbI}_3$  as an absorber layer, which can be used in all other configurations of perovskite solar cells (*e.g.*, planar architecture) in order to further improve the electronic quality of perovskite thin films.

The data underlying this paper are available at: <https://www.repository.cam.ac.uk/handle/1810/260187>.

## Disclosures

The authors declare that they have no competing financial interests.

## Acknowledgements

M. Abdi-Jalebi thanks Nava Technology Limited for a PhD scholarship. M.I. Dar and M.Grätzel thank the King Abdulaziz City for Science and Technology (KACST) and the Swiss National Science Foundation (SNSF) for financial support. The authors would like to thank Dr. Pierre Mettraux in the Molecular and Hybrid Materials Characterization Center, EPFL for carrying out the XPS measurements. A.Sadhanala gratefully acknowledges financial support from the Indo-UK APEX project. S.P. Senanayak acknowledges the Royal Society London for the Newton Fellowship. R.H. Friend, M. Abdi-Jalebi, and A. Sadhanala would like to acknowledge the support from the EPSRC.

## References

- Polman, A., Knight, M., Garnett, E. C., Ehrler, B., & Sinke, W. C. Photovoltaic materials - present efficiencies and future challenges. *Science*. **352**, 307 (2016).
- Green, M. A., Ho-Baillie, A., & Snaith, H. J. The emergence of perovskite solar cells. *Nat. Photonics*. **8** (7), 506-514 (2014).
- Stranks, S. D., & Snaith, H. J. Metal-halide perovskites for photovoltaic and light-emitting devices. *Nat. Nanotechnol.* **10** (5), 391-402 (2015).
- Snaith, H. H. J. Perovskites: The Emergence of a New Era for Low-Cost, High-Efficiency Solar Cells. *The J. Phys. Chem. Lett.* **4** (21), 3623-3630 (2013).
- Kojima, A., Teshima, K., Shirai, Y., & Miyasaka, T. Organometal halide perovskites as visible-light sensitizers for photovoltaic cells. *J. Am. Chem. Soc.* **131** (17), 6050-1 (2009).
- Kim, H.-S., *et al.* Lead iodide perovskite sensitized all-solid-state submicron thin film mesoscopic solar cell with efficiency exceeding 9%. *Sci. rep.* **2**, 591 (2012).
- Jeon, N. J., *et al.* Compositional engineering of perovskite materials for high-performance solar cells. *Nature*. **517** (7535), 476-480 (2014).
- Li, X., *et al.* A vacuum flash-assisted solution process for high-efficiency large-area perovskite solar cells. *Science*. **353** (6294), 58-62 (2016).
- Manser, J. S., & Kamat, P. V Band filling with free charge carriers in organometal halide perovskites. *Nat. Photonics*. **8** (9), 737-743 (2014).
- Xing, G., *et al.* Long-Range Balanced Electron- and Hole-Transport Lengths in Organic-Inorganic  $\text{CH}_3\text{NH}_3\text{PbI}_3$ . *Science*. **342** (6156), 344-347 (2013).
- Stranks, S. D., *et al.* Electron-Hole Diffusion Lengths Exceeding 1 Micrometer in an Organometal Trihalide Perovskite Absorber. *Science*. **342** (6156), 341-344 (2013).
- Pazos-Outon, L. M., *et al.* Photon recycling in lead iodide perovskite solar cells. *Science*. **351** (6280), 1430-1433 (2016).
- Saliba, M., *et al.* Cesium-containing Triple Cation Perovskite Solar Cells: Improved Stability, Reproducibility and High Efficiency. *Energy Environ. Sci.* **9** (6) (2016).
- Pellet, N., *et al.* Mixed-organic-cation perovskite photovoltaics for enhanced solar-light harvesting. *Angew. Chemie - Int. Ed.* **53** (12), 3151-3157 (2014).
- Hao, F., Stoumpos, C. C., Chang, R. P. H., & Kanatzidis, M. G. Anomalous band gap behavior in mixed Sn and Pb perovskites enables broadening of absorption spectrum in solar cells. *J. Am. Chem. Soc.* **136** (22), 8094-9 (2014).
- Dar, M. I., Abdi-Jalebi, M., Arora, N., Grätzel, M., & Nazeeruddin, M. K. Growth Engineering of  $\text{CH}_3\text{NH}_3\text{PbI}_3$  Structures for High-Efficiency Solar Cells. *Adv. Energy Mater.* **6** (2), 1501358 (2016).
- Ibrahim Dar, M., *et al.* Understanding the Impact of Bromide on the Photovoltaic Performance of  $\text{CH}_3\text{NH}_3\text{PbI}_3$  Solar Cells. *Adv. Mater.* **27** (44), 7221-7228 (2015).
- Abdi-Jalebi, M., *et al.* Impact of Monovalent Cation Halide Additives on the Structural and Optoelectronic Properties of  $\text{CH}_3\text{NH}_3\text{PbI}_3$  Perovskite. *Adv. Energy Mater.* **6** (10), 1502472 (2016).
- Yin, W.-J., Shi, T., & Yan, Y. Unusual defect physics in  $\text{CH}_3\text{NH}_3\text{PbI}_3$  perovskite solar cell absorber. *Appl. Phys. Lett.* **104** (6), 063903/1-063903/4 (2014).
- Agiorgousis, M. L., Sun, Y.-Y., Zeng, H., & Zhang, S. Strong Covalency-Induced Recombination Centers in Perovskite Solar Cell Material  $\text{CH}_3\text{NH}_3\text{PbI}_3$ . *J. Am. Chem. Soc.* **136** (41), 14570-14575 (2014).
- Andaji Garmaroudi, Z., Abdi-Jalebi, M., & Mohammadi, M.-R. A facile low temperature route to deposit  $\text{TiO}_2$  scattering layer for efficient dye-sensitized solar cells. *RSC Adv.* (2016).
- Abdi-Jalebi, M., Mohammadi, M. R., & Fray, D. J. Double-Layer  $\text{TiO}_2$  Electrodes with Controlled Phase Composition and Morphology for Efficient Light Management in Dye-Sensitized Solar Cells. *J. of Clust. Sci.* **25** (4), 1029-1045 (2014).



23. Abdi-Jalebi, M., *et al.* Impact of a Mesoporous Titania-Perovskite Interface on the Performance of Hybrid Organic-Inorganic Perovskite Solar Cells. *The J. Phys. Chem. Lett.* **7** (16), 3264-3269 (2016).